Panchromatic (Sub)millimeter Polarization Observations of HL Tau Unveil Aligned Scattering Grains

Zhe-Yu Daniel Lin,[1]
Advisor: Zhi-Yun Li[1]
[1]*Department of Astronomy, University of Virginia, 530 McCormick Rd., Charlottesville 22904, Virginia, USA*

ABSTRACT

Polarization is a unique tool to study the dust grains of protoplanetary disks. Polarization around HL Tau was previously imaged using the Atacama Large Millimeter/submillimeter Array (ALMA) at Bands 3 (3.1 mm), 6 (1.3 mm), and 7 (0.87 mm), showing that the polarization orientation changes across wavelength λ. Polarization at Band 7 is predominantly parallel to the disk minor axis but appears azimuthally oriented at Band 3, with the morphology at Band 6 in between the two. We present new $\sim 0.2''$ (29 au) polarization observations at Q-Band (7.0 mm) using the Karl G. Jansky Very Large Array (VLA) and at Bands 4 (2.1 mm), 5 (1.5 mm), and 7 using ALMA, consolidating HL Tau's position as the protoplanetary disk with the most complete wavelength coverage in dust polarization. The polarization patterns at Bands 4 and 5 follow the previously identified morphological transition with wavelength. From the azimuthal variation, we decompose the polarization into contributions from scattering (s) and thermal emission (t). s decreases slowly with increasing λ, and t increases more rapidly which are expected from optical depth effects of toroidally aligned, scattering prolate grains. The weak λ dependence of s is inconsistent with the simplest case of Rayleigh scattering by small grains in the optically thin limit but can be affected by factors such as optical depth, disk substructure, and dust porosity. The sparse polarization detections from the Q-band image are also consistent with toroidally aligned prolate grains.

1 INTRODUCTION

Studying the dust properties of protoplanetary disks is crucial for understanding the origins of planets, because dust grains serve as the building blocks of planet formation (e.g. Beckwith et al. 2000; Johansen et al. 2014; Morbidelli & Raymond 2016). Polarization at millimeter wavelengths has emerged as a unique and powerful tool for studying the properties of dust grains and their initial conditions in disks (e.g. Andersson et al. 2015; Kataoka et al. 2015). With the advent of the Atacama Large Millimeter/submillimeter Array (ALMA), the field of (sub)millimeter-wavelength disk polarization has witnessed a revolution, thanks to the unprecedented sensitivity and spatial resolution (e.g. Kataoka et al. 2016b; Stephens et al. 2017; Alves et al. 2018; Lee et al. 2018; Girart et al. 2018; Bacciotti et al. 2018; Dent et al. 2019; Takahashi et al. 2019; Harrison et al. 2019; Sadavoy et al. 2019; Harrison et al. 2021; Ohashi et al. 2020; Stephens et al. 2020; Lee et al. 2021; Aso et al. 2021; Tang et al. 2023).

A common process to produce disk polarization is through dust scattering. Grains can efficiently scatter thermal radiation from other grains when the sizes of grains become comparable to the observing wavelength (Bohren & Huffman 1983; Kataoka et al. 2015). This mechanism produces a distinctive pattern in an inclined disk where the polarization direction is parallel to the disk minor axis (Yang et al. 2016a; Kataoka et al. 2016a). Most sources with resolved disk-scale polarization observations show this pattern (e.g. Stephens et al. 2014, 2017; Hull et al. 2018; Takahashi et al. 2019) and the measurements of the spectral index of Stokes I support the dust scattering interpretation (e.g. Zhu et al. 2019; Liu 2019; Carrasco-González et al. 2019; Lin et al. 2020b).

Another process to produce polarization is through polarized thermal emission of aligned, elongated grains. There are several proposed mechanisms to align grains, including radiative alignment torques (RAT; Dolginov & Mitrofanov 1976; Draine & Weingartner 1997), mechanical alignment torques (MET; Gold 1952; Lazarian & Hoang 2007; Hoang et al. 2018), or paramagnetic alignment, which can align grains either to the magnetic field, radiation field, or the gas flow depending on the details of each mechanism (see e.g., Andersson et al. 2015; Hoang et al. 2022). While grains are likely aligned to the magnetic field in the diffuse ISM and protostellar envelopes through RAT or its magnetically enhanced version MRAT (e.g. Hoang & Lazarian 2016; Le Gouellec et al. 2020; Valdivia et al. 2022), it is unclear which mechanism can align grains in protoplanetary disks. Nevertheless, one can infer the presence of aligned grains through a consistent polarization pattern across wavelengths (Cox et al. 2015; Alves et al. 2018) or through a 90° flip due to dichroic extinction (Ko et al. 2020; Lin et al. 2020a; Liu 2021).

Interestingly, in some disks, polarization measurements exhibit polarization consistent with dust scattering at shorter wavelengths, but the polarization becomes azimuthally oriented at longer wavelengths (e.g. Stephens et al. 2017; Harrison et al. 2019; Mori et al. 2019; Harrison et al. 2021). The difference in the polarization patterns is not expected from scattering or aligned grains alone (Yang et al. 2016b; Stephens et al. 2017; Yang et al. 2017; Mori & Kataoka 2021). The best-studied case, thus far, that exhibits the transition in disk-scale polarization morphology with wavelength is HL Tau, a Class I/II protostar. At Band 3 the polarization is azimuthally oriented with $\sim 2\%$ polarization (Kataoka et al. 2017). At Band 7, the polarization becomes unidirectional and parallel to the disk minor axis with $\sim 0.8\%$ polarization (Stephens et al. 2014, 2017). Intriguingly, the Band 6 image has polarization directions that are in between the two extremes (Stephens et al. 2017).

Studies have shown that the azimuthally oriented polarization at Band 3 seen in HL Tau is better explained by toroidally aligned effectively prolate grains than radially aligned effectively oblate grains based on the azimuthal variation of polarization (Kataoka et al. 2017; Yang et al. 2019; Mori & Kataoka 2021). Realistic grains are likely irregular and triaxial in general. We use prolates and oblates as a simplified representation of the ensemble average of the grains with, respectively, their long and short axes aligned systematically. By self-consistently solving radiation transfer equations, including the thermal polarization and scattering of aligned grains, Lin et al. (2022) demonstrated that the transition in polarization morphology could be attributed to an increase of optical depth towards shorter wavelengths that causes scattering polarization to dominate over the polarization from the underlying thermal polarization of aligned grains. The optical depth interpretation also naturally explains the Band 6 image that appears in between the two extreme morphology if the optical depth is largely in between that at Bands 3 and 7. To further test if toroidally aligned prolate grains with varying optical depth can explain the polarization transition, we need additional resolved polarization observations at different wavelengths.

HL Tau is located in the L1551 dark cloud of the Taurus-Auriga molecular cloud complex (Kenyon et al. 2008). The conventional adopted distance for the cloud complex is 140 pc (Kenyon et al. 1994), but recent advancements in distance measurement have revealed a significant line of sight depth (Loinard 2013). Studies utilizing Gaia data have reported distances of 145 pc (Luhman 2018) and 146 ± 0.6 pc (Roccatagliata et al. 2020). Additionally, the Very Long Baseline Array yielded a distance of 147.3 ± 0.5 pc (Galli et al. 2018). We adopt a distance of 147.3 pc for HL Tau for consistency with the recent high angular resolution study (Carrasco-González et al. 2019).

In this paper, we present new polarization observations at Bands 4 and 5 using ALMA and Q-Band using the Very Large Array (VLA) to investigate whether the observed transition in polarization extends to other wavelengths. We also present a new ALMA Band 7 polarization image with improved angular resolution and reprocessed previous ALMA Bands 3 and 6 data gathering a final set of images with comparable angular resolution. By obtaining multiwavelength polarization images, we aim to confirm the presence of the transition and test predictions from optical depth effects (Lin et al. 2022). The paper is organized as follows: In Section 2, we provide a brief overview of the observations and the data calibration procedure. Section 3 presents our results, showcasing the polarization properties of HL Tau at different wavelengths, and we analyze the polarization across wavelengths in Section 4. We discuss the implications of our results in Section 5 and summarize in Section 6.

2 OBSERVATIONS

To date, HL Tau has been observed by ALMA at Bands 3 (3.09 mm), 4 (2.07 mm), 5 (1.48 mm), 6 (1.29 mm), and 7 (0.87 mm) and by the VLA at Q-band (6.97 mm). Bands 3 (project code: 2016.1.00115.S; PI: Akimasa Kataoka) and 6 (project code: 2016.1.00162.S; PI: Ian Stephens) data were first presented in Kataoka et al. (2017) and Stephens et al. (2017), respectively, but we reimaged the measurement sets after self-calibration. While Band 7 was originally presented in Stephens et al. (2017), we used deeper and higher resolution data from Stephens et al. (2023) (project code: 2019.1.01051.S; PI: Ian Stephens). The calibration settings are listed in Lin et al. (2024). We used the Common Astronomy Software Applications (CASA) package for all calibration and imaging on the ALMA and VLA data (McMullin et al. 2007).

2.1 ALMA Observations

For all the ALMA data presented in this paper, including archival and new data, we self-calibrated and imaged the data for all 5 bands so that they would all be imaged in a consistent manner. Before self-calibration, we re-ran the data through ALMA's calibration pipeline using the ALMA-supplied calibration scripts. These scripts do the standard calibration, which includes bandpass, phase, polarization, and flux calibration.

We use *tclean* for imaging and use the Briggs robust parameter of 0.5 for each wavelength. The data from every band went through three rounds of phase-only self-calibration, with solution intervals *infinity*, 30.5 s, and 10.4 s. Final deep cleaning of the four Stokes parameters using a cleaning mask covering the HL Tau disk area led to signal-to-noise ratios of $\sim$ 1200, 890, 1200, 1100, and 1300 from Bands 3 to 7, respectively. The detailed calibration procedure and resulting noise levels are listed in Lin et al. (2024).

2.2 VLA Q-band Observations

We observed HL Tau with the VLA in its B configuration during three semesters (Legacy project code: 19A-388). We completed eight observation epochs between May 2019 to September 2021 (2 in 2019, 5 in 2020, and 1 in 2021). We used the usual continuum frequency setup covering a frequency range 39-47 Hz, and full polarization mode. In each epoch, the total observing time was 5 hours with 2.5 hours on target. For the calibration of the data, we used CASA and a modified version of the National Radio Astronomy Observatory (NRAO) Pipeline which includes polarization calibration after the usual gain calibration. For the calibration of the polarization angle, we used the known polarization parameters for 3C147, i.e., a polarization angle of 86° and a polarization degree of 5.2% (Perley & Butler 2013). We assumed these parameters to be constant across the 8 GHz bandwidth of the Q band observations (see Lin et al. (2024) for details). The final images were made using *tclean* and a natural weighting. The signal-to-noise ratio of the peak I is 210. The resulting synthesized beam size is $0.156'' \times 0.143''$.

2.3 Construction of Polarization Images

The noise levels for each Stokes parameter, I, Q, U, and V, are denoted as σ_I, σ_Q, σ_U, and σ_V, respectively, and are listed in Lin et al. (2024) in detail. F_ν is the flux density of Stokes I where we use emission above 3 σ_I. We assume a 10% absolute calibration uncertainty based on the VLA and the ALMA technical handbooks, but we ignore it for the rest of the paper.

In the ideal limit without noise, the linear polarized intensity is directly related to Stokes Q and U through:

$$P_m \equiv \sqrt{Q^2 + U^2}. \tag{1}$$

However, when including noise, Eq. (1) results in a positive bias, because the Stokes Q and U can be positive or negative while the linear polarized intensity is always positive.

Following Vaillancourt (2006) and Hull & Plambeck (2015), we de-bias the linear polarized intensity by considering the probability density function (PDF):

$$\mathrm{PDF}(P|P_m, \sigma_P) = \frac{P}{\sigma_P^2} I_0\left(\frac{P P_m}{\sigma_P^2}\right) \exp\left[-\frac{(P_m^2 + P^2)}{2\sigma_P^2}\right] \tag{2}$$

which describes the probability of the true linear polarized intensity P given a measured P_m and noise level σ_P. I_0 is the zeroth-order modified Bessel function of the first kind. σ_P comes from σ_Q and σ_U which are usually comparable, but we define the noise level of the linear polarized intensity through

$$\sigma_P = \sqrt{(\sigma_Q^2 + \sigma_U^2)/2} \tag{3}$$

as an explicit way to account for any slight difference. Thus, we obtain P by finding the maximum of Eq. (2). For high signal-to-noise detections ($P_m \geq 5\sigma_P$), a simple approximation exists:

$$P = \sqrt{Q^2 + U^2 - \sigma_P^2}, \tag{4}$$

but we use Eq. (2) for $P_m < 5\sigma_P$.

The sign of the Stokes parameters follows the IAU convention (Contopoulos & Jappel 1974; Hamaker et al. 1996; Hamaker & Bregman 1996). The polarization angle is defined by

$$\chi \equiv \frac{1}{2}\arctan\left(\frac{U}{Q}\right) \tag{5}$$

and goes East-of-North. We only consider the E-vectors, whose angles are defined by Eq. (5) and not the B-vectors (rotated by 90°) that are conventionally used to trace the magnetic field assuming aligned oblate grains. The uncertainty of χ is

$$\sigma_\chi = \frac{1}{2}\frac{\sigma_P}{P} \tag{6}$$

(Hull & Plambeck 2015).

We further define several convenient quantities. The linear polarization fraction is

$$p \equiv \frac{P}{I}. \tag{7}$$

In addition, the Stokes Q and U normalized by Stokes I are $q \equiv Q/I$ and $u \equiv U/I$, where we use lowercase to represent quantities of polarized intensity normalized by Stokes I.

The uncertainty of p is

$$\sigma_{\rm pf} = \frac{P}{I}\sqrt{\left(\frac{\sigma_P}{P}\right)^2 + \left(\frac{\sigma_I}{I}\right)^2} \tag{8}$$

which is estimated through error propagation. We note that the ALMA technical handbook gives a minimum detectable degree of polarization, which is defined as three times the systematic calibration uncertainty, of 0.1% for compact sources within the inner third of the primary beam. Thus, we use the error of 0.033% whenever the error from Eq. (8) is less than this value for data from ALMA. The uncertainties of q and u are likewise estimated through error propagation.

3 RESULTS

3.1 Polarization Morphology

Fig. 1 shows the polarization images across all six bands. There exists a consistent transition in the polarization morphology across the spectrum. Starting from the longest wavelength with Fig. 1a, the VLA Q-Band only marginally detected a few vectors (E-vectors). Although there are a few regions with P above $3\sigma_P$ in the image, we only consider polarization detections where Stokes I is also detected above $3\sigma_I$. The vector closest to the center is $\sim$ 4% and appears parallel to the disk major axis. The other vectors are $\sim$ 10% and are oriented azimuthally around the center.

The image at λ=3.1 mm (Band 3) shows an azimuthal distribution of P around a center of low P with two null points to the East and West of the center. The polarization direction (E-vectors) is oriented azimuthally around the center in that the polarization along the major axis is parallel to the disk minor axis and that along the minor axis is parallel to the disk major axis. In addition, the polarization fraction p is larger at larger radii. These characteristics are qualitatively consistent with Kataoka et al. (2017) and Stephens et al. (2017) where the data originally appeared. The resolution of $\sim 0.35''$ in this work is similar to that in Kataoka et al. (2017) which also used robust=0.5 and is slightly better than the resolution of $\sim 0.46''$ in Stephens et al. (2017) which used robust=1.0.

The image at 2.1 mm (Band 4) appears similar to the Band 3 image in that P is azimuthally distributed around the center and the polarization vectors are also directed azimuthally. The main difference is that P is slightly separated into two lobes along the major axis of the disk, whereas P at Band 3 appears relatively more uniform.

The 1.5 mm (Band 5) image shows a more obvious change in the distribution of P and in the polarization angle. P is clearly stronger along the major axis than along the minor axis. The two lobes along the major axis are more obvious and a weak link at the center emerged, forming a "dumbbell" shape. Along the disk minor axis, we detect polarization in the northeast (beyond the null point) with polarization parallel to the disk major axis, while P at the corresponding location in the southwest is less well detected.

At 1.3 mm (Band 6), the image also shows a stronger P along the major axis than along the minor axis, with a prominent dumbbell shape similar to that at Band 5. Also, the polarization vectors are clearly no longer directed azimuthally like at 3.1 mm. Instead, the vectors around the northeast edge and the southwest edge appear tilted towards the disk minor axis. The Band 6 image in this work is qualitatively similar with Stephens et al. (2017) where the data originally appeared, but differs in angular resolution in that the previous work used robust=1.0. We also better detect P in the northeastern part of the disk minor axis resulting in a reduced null point.

At 870 μm (Band 7), P is distributed across the disk without any null points and the polarization is mostly parallel to the disk minor axis with slight deviations that resemble the elliptical pattern at longer wavelengths. The resolution is better than the one in Stephens et al. (2017) ($\sim 0.39''$). The high polarization vectors in the southwest location in Stephens et al. (2017) do not appear in the new image which could suggest a spurious detection. The uniform polarization morphology across the disk is similar to the polarization expected from scattering in an inclined disk (Yang et al. 2016a).

4 POLARIZATION ANALYSIS

From Section. 3, we find a systematic transition of the polarization angle from being uniformly parallel to the disk minor axis at the shortest wavelength to being azimuthally oriented around the center at the longest wavelength. To quantify the transition, we follow the technique developed from Lin et al. (2022) which disentangles the azimuthal variation of polarization from a constant component. The technique relies on the approximation that scattering mainly produces a constant polarization due to inclination, thermal polarization produces the azimuthal variation, and both quantities add linearly based on polarized radiation transfer calculations in a simplified plane-parallel geometry.

In the following, Section 4.1 describes a particular reference frame to analyze the Stokes Q and U in a standardized way. Using Stokes Q and U instead of P is beneficial since they retain the information on both the level of polarization and the direction. Section 4.2 introduces the linear decomposition method and measures the spectrum of the scattering component and thermal component.

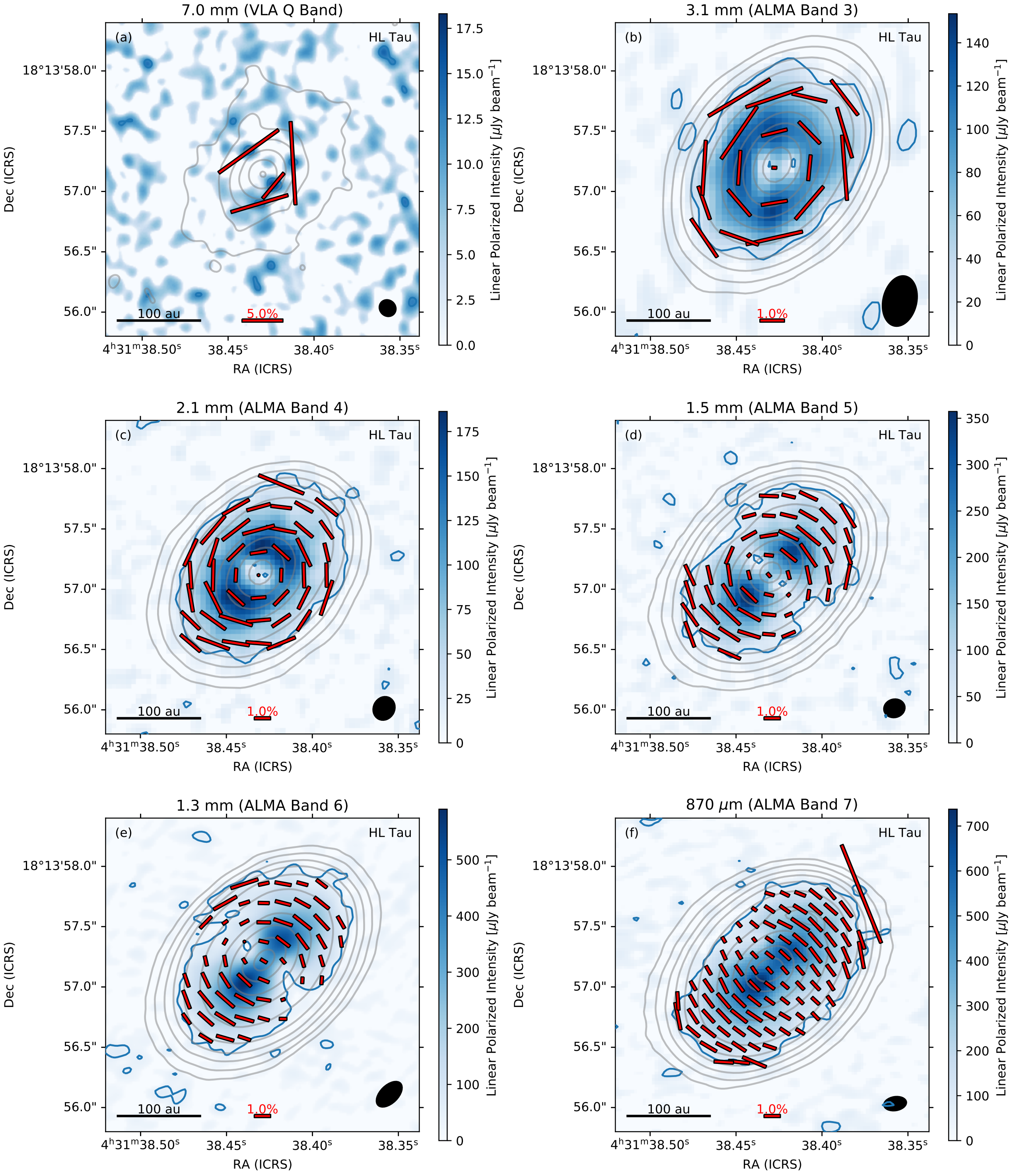

Figure 1. Panels a to f show the polarimetric data from the VLA Band Q and ALMA Bands 3, 4, 5, 6, and 7, respectively. In each panel, the color map represents the linear polarized intensity in μJy beam^{-1}. The blue contour traces the $3\sigma_P$ level, while grey contours show the Stokes I in steps of 3, 10, 25, 50, 100, 200, 325, 500, 750, and 1000 σ_I. The direction of the red line segments represents the polarization angle, while the length of the line segments is proportional to the linear polarization fraction. Each line segment samples the image in step sizes equal to the FWHM of the minor axis of the beam. The length of 1% polarization is shown in the center bottom. The black bar to the bottom left shows the 100 au scale. The black ellipse to the bottom right represents the synthesized beam.

4.1 Principal Frame View

Stokes Q and U depend on the orientation of the image frame. We define an image frame with coordinates x and y, such that the x- and y-axes are along the disk minor and major axes, respectively. Since there is a 180° ambiguity in the direction of x (and, likewise, y), we arbitrarily fix the positive x-direction to the far side of the disk. The positive y-direction is 90° (East-of-North) from that. We use the term "principal" frame, since it is oriented along the principal axes (i.e., major and minor axes) of an inclined axisymmetric disk.

The Stokes Q' and U' defined in the principal frame (denoted with a prime) follow the usual definition from the Institute of Electrical and Electronics Engineering (IEEE Standard 211, 1969) which is the basis of the IAU convention (Contopoulos & Jappel 1974; Hamaker et al. 1996; Hamaker & Bregman 1996). Let ϕ be the angle in the image plane from the positive x-axis that increases in the counter-clockwise direction (in the same direction as going East-of-North). Positive Q' is polarization along x ($\phi = 0°$) and positive U' is polarization along the bisectrix of the positive x and y axes ($\phi = 45°$). Note that the coordinate system is different from the definition adopted in Lin et al. (2022), and we provide the derivation of the principal frame that strictly follows the IEEE definition. This frame is motivated by the fact that the scattering of an inclined disk largely produces unidirectional polarization parallel to the disk minor axis, which would show as positive Stokes Q' and zero Stokes U'.

Under this definition, Stokes Q' and U' are related to the Stokes Q and U in the original sky frame with a simple rotation. We use ΔRA and ΔDec as the coordinates in the original sky frame with respect to the center of the disk. In the sky frame, let η be the position angle (East-of-North) of the minor axis of the disk that corresponds to the far side (i.e., the positive direction of the x-axis). The coordinates in the principal frame are related to the sky frame by

$$\begin{pmatrix} x \\ y \end{pmatrix} = \begin{pmatrix} \cos\eta & \sin\eta \\ -\sin\eta & \cos\eta \end{pmatrix} \begin{pmatrix} \Delta\mathrm{Dec} \\ \Delta\mathrm{RA} \end{pmatrix}. \tag{9}$$

The Stokes Q and U in the sky frame are related to the Stokes Q' and U' of the principal frame by

$$\begin{pmatrix} Q' \\ U' \end{pmatrix} = \begin{pmatrix} \cos 2\eta & \sin 2\eta \\ -\sin 2\eta & \cos 2\eta \end{pmatrix} \begin{pmatrix} Q \\ U \end{pmatrix}. \tag{10}$$

The definition of η is different from the position angle of the disk major axis that is usually reported. The position angle of the disk major axis is 138.02° based on high angular resolution images from ALMA Partnership et al. (2015). The far side of the disk is to the northeast since the outflow direction is blueshifted to the northeast and redshifted to the southwest (ALMA Partnership et al. 2015; Yen et al. 2017). Thus, we have $\eta = 48.02°$.

Stokes Q' and U' images are shown in Fig. 2. For direct comparison, we also show Stokes I in the principal frame, which is equal to Stokes I in value but simply rotated. We can easily understand the multiwavelength transition in this frame (at least for the well-detected ALMA images). Across wavelength, from Band 3 (3.1 mm) to Band 7 (870μm), Stokes Q' shifts from a petal pattern with alternating signs in each quadrant to an image that is entirely positive. Stokes U' is mostly zero along the principal axes and the petal pattern with alternating signs does not change with wavelength as Stokes Q' does.

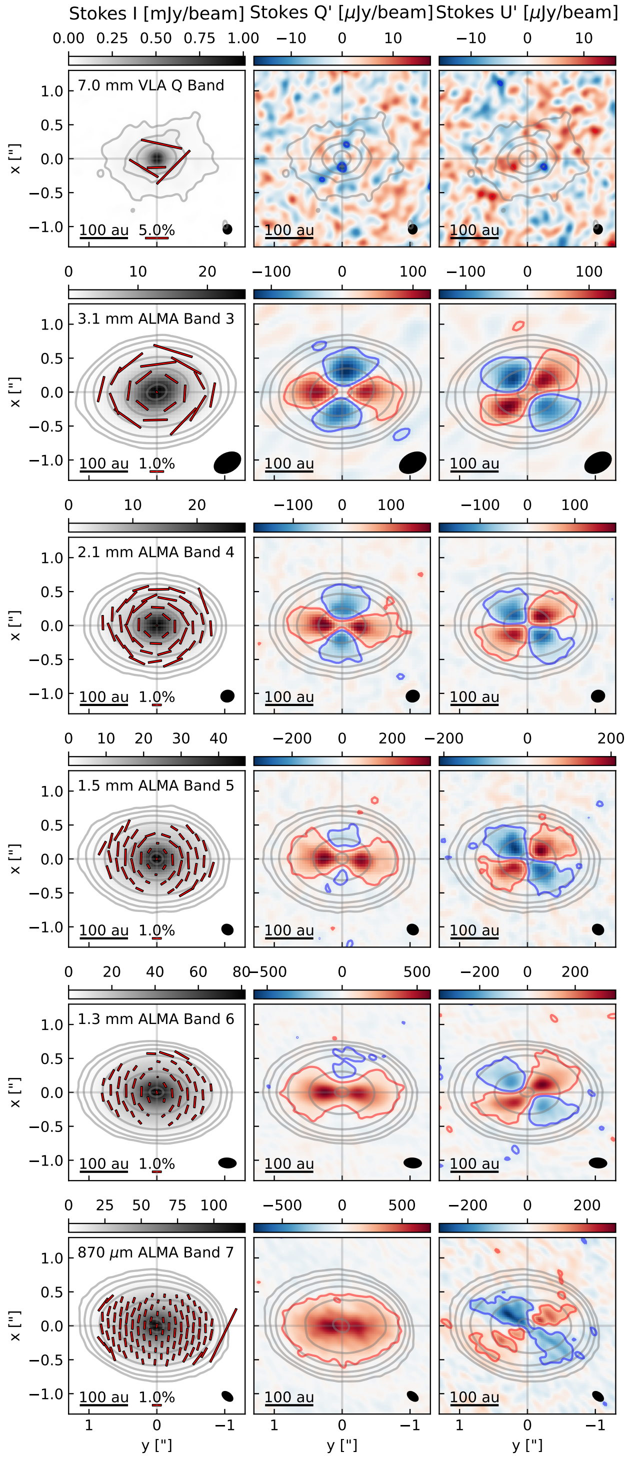

Figure 2. Stokes I, Q', and U' at each band where Q' and U' are Stokes Q and U rotated to the principal frame. I, Q', and U' images go left to right, while bands Q, 3, 4, 5, 6, and 7 go from the top to the bottom row. The vertical axis (x-axis) of the image is along the disk minor axis with $x > 0$ defined to be along the far side. The horizontal axis (y-axis) is along the disk major axis. The line segments on top of the Stokes I images represent the polarization direction and the segment length is proportional to p where the scale bar is shown at the bottom. The color scales of Stokes Q' and U' are plotted such that the white corresponds to the zero level. The -3σ and 3σ levels are marked by blue and red contours respectively. The synthesized beam is represented as a black ellipse to the lower right of each plot.

4.2 Linear Decomposition

4.2.1 Methodology

Solving the polarized radiation transfer equation including polarized thermal emission and scattering of elongated grains self-consistently is notoriously challenging (e.g. Steinacker et al. 2013). Nevertheless, as demonstrated by Lin et al. (2022), the problem simplifies significantly in a plane-parallel slab. Since the dust layer responsible for the HL Tau (sub)millimeter continuum is geometrically thin (Pinte et al. 2016), one can approximate each local patch of the dust disk as a plane-parallel slab.

In addition, Lin et al. (2022) found that, when the optical depth is less than of order unity, the polarization fraction is approximately a linear addition of polarization due to thermal emission of the elongated grain without scattering and polarization due to scattering of a volume-equivalent sphere when the shape of the grain is nearly spherical. When the optical depth is large, the resulting polarization fraction is largely determined by scattering alone. The approximation enables us to sidestep complications arising from the full disk geometry and (uncertain) grain opacities and directly estimate the contributions from scattering and thermal emission from the azimuthal variation. We limit the model to the ALMA Bands since the polarization is better detected around the full azimuth.

For clarity, we provide the essential derivation with the appropriate convention adopted in this work (see Lin et al. 2022 for the original derivation). Assuming a prolate grain in the dipole limit, the polarization purely from thermal emission is (Lee & Draine 1985; Yang et al. 2016b):

$$p(\theta_g) = \frac{p_0 \sin^2 \theta_g}{1 - p_0 \cos^2 \theta_g} \approx p_0 \sin^2 \theta_g \tag{11}$$

where θ_g is the viewing angle from the axis of symmetry of the grain ($\theta_g = 0^\circ$ means the grain is seen pole-on). Recall that the use of a lowercase refers to a quantity that is related to the polarization fraction (normalized by I). We define p_0 as the intrinsic polarization, which is the polarization of the grain seen edge-on ($\theta_g = 90^\circ$) and is the maximum polarization possible just from the shape if the grains are perfectly aligned in the same direction. The approximation to the right-hand-side of Eq. (11) applies because $p_0 \ll 1$.

Since HL Tau is a relatively evolved source without a massive envelope that can significantly modify the disk polarization, we consider only the emission and extinction by the grains in the disk. Dichroic extinction attenuates the polarization as optical depth increases (e.g. Hildebrand et al. 2000; Lin et al. 2022). Since $p_0 \ll 1$, the resulting polarization remains $\propto p_0 \sin^2 \theta_g$, so we express the thermal polarization as

$$t_p(\theta_g) = t \sin^2 \theta_g \tag{12}$$

where t is p_0 attenuated by optical depth. The explicit dependence of t on optical depth can be complicated and is beyond the scope of this paper, but the usefulness of Eq. (12) is in separating the optical depth attenuation part from the part that only depends on the viewing angle (which gives the azimuthal variation as we see below). We should note that the parameter t can, in principle, be negative, which happens when the dichroic extinction polarization overwhelms the emission polarization and flips the polarization orientation by 90°. However, for a dust layer in the disk, a significant temperature gradient along the line of sight through the layer is required to produce the 90° polarization flip by extinction (e.g. Yang et al. 2017; Lin et al. 2020a). Since the relatively large grains responsible for the (sub)mm continuum emission in the HL Tau disk are known to have settled to a thin layer near the midplane (e.g. Kwon et al. 2011; Pinte et al. 2016), little temperature variation is expected along the sightline through the dust layer. In this case, the polarization fraction of the dust thermal emission will decrease monotonically with increasing optical depth, and its orientation will not flip by 90° as the optical depth increases (consistent with the positive values of the parameter t obtained from fitting the observation data in Section 4.2.2 below).

Next, we consider an inclined axisymmetric disk demonstrated. Let Z be the rotation axis of the disk and $\mathbf{n}$ be a unit vector directed to the observer. The inclination i is the angle between Z and $\mathbf{n}$. X and Y are axes in the disk midplane such that X is coplanar to Z and $\mathbf{n}$. We define Φ as the azimuthal angle in the disk midplane from the X-axis without loss of generality since the disk is assumed to be axisymmetric. The alignment axes of the prolate grains are in the disk midplane and in the azimuthal direction. Based on the definition of the principal frame in Sec. 4.1, x is in the XZ-plane. For convenience, we define ϕ as the azimuthal angle in the image plane from the x-axis.

Let $q' \equiv Q'/I$ and $u' \equiv U'/I$ (i.e., normalized Q' and U' in the principal frame). Depending on the location along the azimuth, the viewing angle θ_g varies and gives the azimuthal variation seen in the image. The polarization from the scattering component, which we denote as s, is largely constant of azimuth and only contributes to q' since the inclination-induced polarization is always parallel to the disk minor axis. Adding the thermal component and scattering component together, we get

$$q' = s + t(\cos^2 i \sin^2 \Phi - \cos^2 \Phi) \tag{13}$$

$$u' = -t \cos i \sin 2\Phi. \tag{14}$$

Using Eq. (13) and (14) we fit the azimuthal profile of q' and u', respectively, at 100 au first for each ALMA band. We exclude the Q-band data because the polarization detections lack enough azimuthal coverage and, in addition, the low signal-to-noise does not permit reliable results. The chosen radius is $\sim$ 2 beams away from the center for the Band 3 image, which has the poorest resolution, to minimize the effects of beam convolution, but is also within a range with enough signal-to-noise for all five bands. We conduct the same process for other radii below. Sampling the azimuthal profile uses steps equal to the geometric average of the beam size.

We use *emcee*, a Monte Carlo Markov Chain sampling code (Foreman-Mackey et al. 2013), to find the best-fit values and uncertainties of s and t at each wavelength. We use 32 walkers and a total of 2500 steps. We ignore the first 500 steps to obtain the posterior probability distribution. Modifying the walking parameters does not significantly change the results. The best-fit values are determined from the median of the marginalized distribution, and the 1σ uncertainties use the 16th and 84th percentile.

4.2.2 Results

Fig. 3 shows the best-fit curve of the model compared to the sampled observational data points for the high signal-to-noise ALMA observations. We find that the linear decomposition model describes all five bands, in both q' and u', remarkably well considering the simplicity of the model. While this was already shown for the same Bands 3 and 6 data with just a difference in the self-calibration and imaging procedure (Lin et al. 2022), it is reassuring to see that the new Bands 4, 5, and 7 data follow the same pattern, which adds weight to the validity of the simple decomposition technique. Intriguingly, q' of the near side ($\Phi \in [90^\circ, 270^\circ]$) appears slightly, but systematically larger than the best-fit model, while q' of the far side ($\Phi \in [-90^\circ, 90^\circ]$) appears systematically lower, indicating another, more secondary effect is also at play.

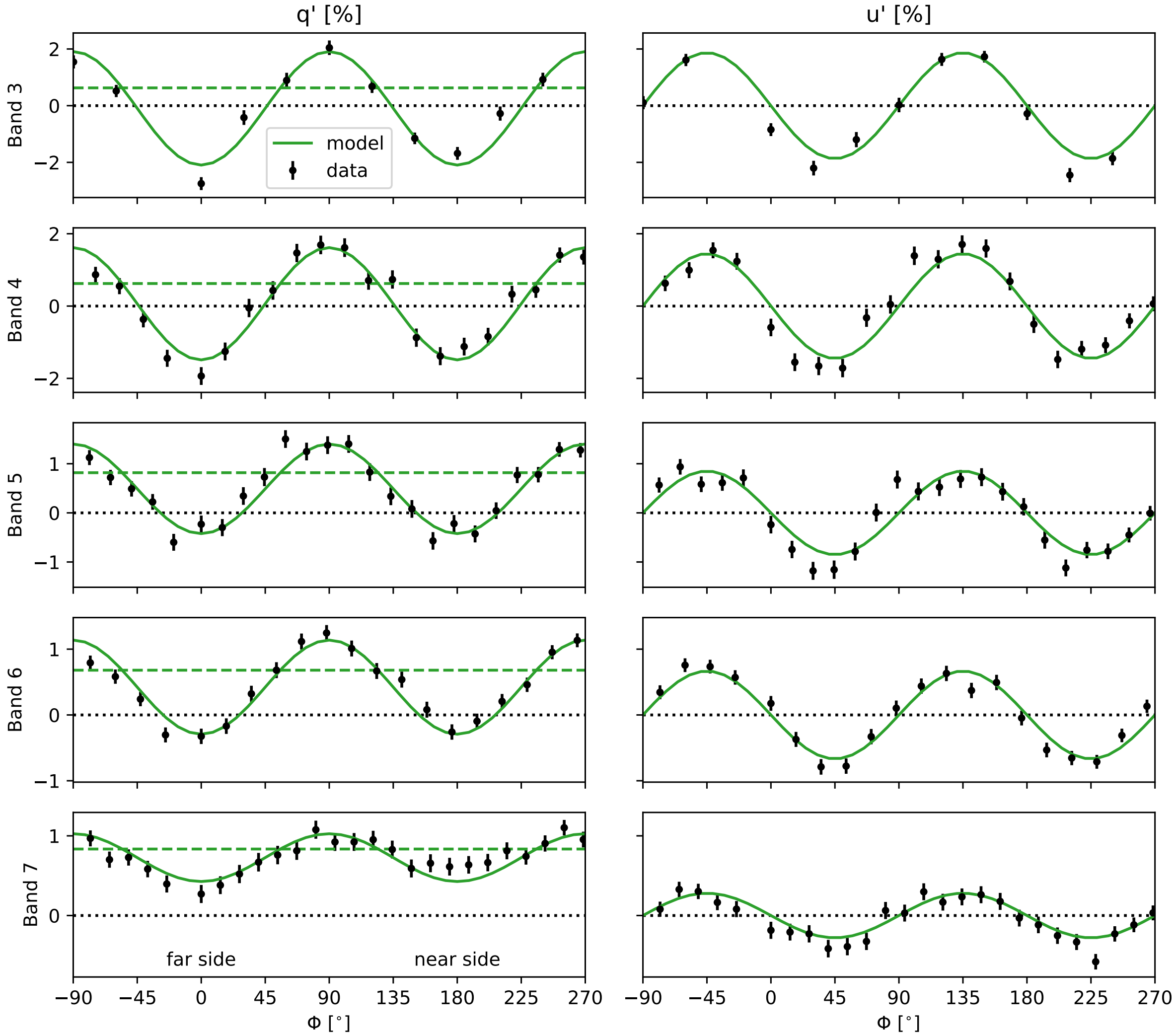

Figure 3. The azimuthal variation of q' and u' (left and right columns) for each ALMA Band (from top to bottom). The data are shown in black dots with error bars corresponding to the statistical uncertainty. The green curves are the best-fit model curves, and the green horizontal dashed curve in the left panels is the best-fit s component. The black horizontal dotted curve is the zero line. Φ is plotted from -90° to 270° to better see the complete near and far sides.

Fig. 4a shows the best-fit s and t as a function of wavelength including the uncertainties estimated from *emcee*. Evidently, the contribution from thermal polarization, t, monotonically increases with increasing wavelength. The behavior is consistent with what we expect from a decrease in optical depth as the dust opacity decreases towards longer wavelengths (Hildebrand et al. 2000; Yang et al. 2017). Indeed, previous studies have found that the optical depth decreases towards longer wavelength (Pinte et al. 2016; Carrasco-González et al. 2019).

The contribution from scattering, s, slowly decreases with increasing wavelength in general with the exception of s at λ=1.5 mm (Band 5) which appears slightly larger than s at $\lambda = 1.3$ mm (Band 6). To describe the spectrum of the scattering component, we fit a power-law in the form of $a(\lambda/1\text{mm})^b$. We again use *emcee* and obtain $a \sim 0.796 \pm 0.016$ % and $b \sim -0.26 \pm 0.06$. The overall decrease of s (negative b) is what we expect due to decreasing optical depth. How slowly s decreases may depend on the optical depth, opacity index, grain size, and porosity which we discuss in Section 5.

The slight increase of s at Band 5 could be due to the maximized scattering (inclination-induced) polarization when the optical depth is of order unity (Yang et al. 2017; Lin et al. 2022). Multiwavelength continuum ray-tracing from Pinte et al. (2016) showed that, at a radius of 100 au, the optical depths at Band 3 (2.9 mm) and 6 (1.3 mm) are $\sim$ 0.4 and 0.3, respectively, though the modeling did not consider scattering. Nevertheless, including scattering, Carrasco-González et al. (2019) obtained optical depths of $\sim$ 1 and $\sim$ 3 at Bands 4 (2.1 mm) and 6 (1.3 mm), respectively, at the same radius. Band 5 (1.5 mm), being in between the wavelengths considered in the previous two studies, appears likely to have an optical depth necessary to maximize the inclination-induced polarization.

We note that when comparing properties across wavelengths, it is preferable to use the same spatial resolution. Thus, we conduct the same procedure at the same radius, but with all the data convolved to the same resulting beam size using the CASA *imsmooth* task. We use the beam size from Band 3 which is the largest among the five bands.

The resulting s-spectrum (Fig. 4b) is comparable to the original profile, which is reasonable since scattering polarization is largely

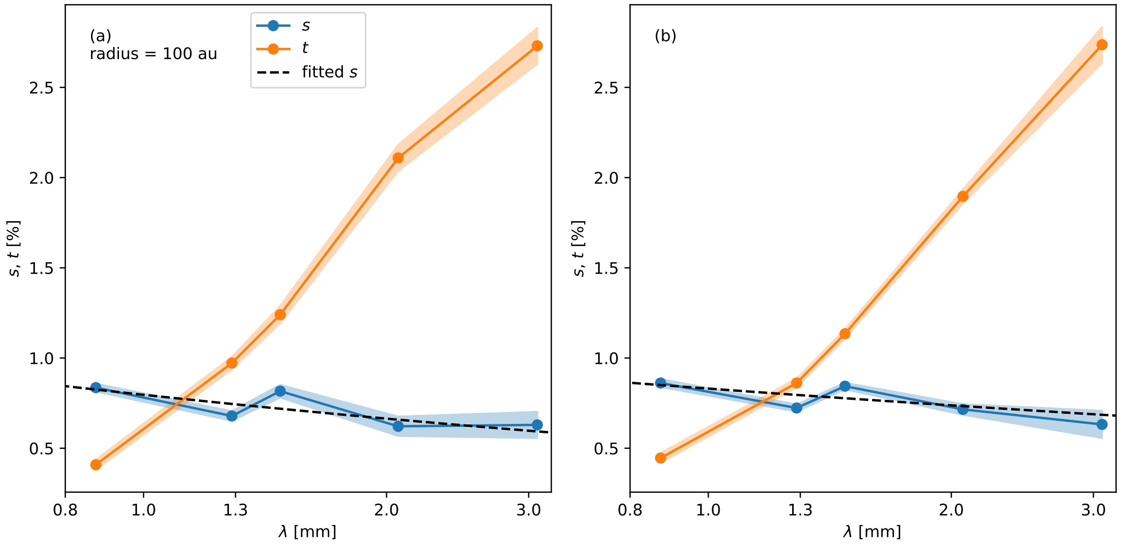

Figure 4. The spectrum of s and t: s is the level of polarization from scattering, while t is the intrinsic polarization from aligned grains attenuated by optical depth. Panel (a): The results from fitting the data at their native resolution. Panel (b): The results from fitting the data after convolving Bands 4 to 7 with smaller beam sizes to the Band 3 beam size. The blue and orange curves are s and t, while the shaded regions represent the 1σ uncertainty from the fit. The dashed line is the best-fit power-law curve to the s spectrum.

unidirectional and the averaging effects from a moderately larger beam will not introduce significant cancellations. Indeed, by fitting the s spectrum, we get $a = 0.831 \pm 0.016\%$, $b = -0.17 \pm 0.05$, which is comparable to the values obtained in the previous case. The resulting t-spectrum (Fig. 4a) remains monotonically increasing with wavelength and does not change significantly from Fig. 4a) However, the slight drop in t (most clearly seen at Band 4) after convolution is because of the beam cancellation of its azimuthal polarization.

4.3 Q-Band consistency with toroidally aligned grains

Using the longest wavelength, VLA Q-band data, we check if the polarization angles, χ, are consistent with toroidally aligned prolate grains. Following Sections 4.1 and 4.2, we can deproject the location of the detected vectors and derive the expected χ from toroidally aligned prolate grains. We use Eq. (13) and (14), but assume $s = 0$ to derive the χ in the principal frame and rotate it to the sky frame.

Fig. 5 shows the Q-Band polarization image compared to the expected polarization direction. The differences with the observed χ normalized by the σ_χ are 0.5, -0.4, 0.4, and 0.08, which means the observed χ are consistent with toroidally aligned prolate grains. In addition, the probability for random noise to have 4 points within $\pm 1\sigma_\chi$ of the expected polarization direction is $\Pi_{i=1}^{4} 2\sigma_{\chi,i}/180° \sim 7 \times 10^{-5}$, where $\sigma_{\chi,i}$ represents the σ_χ of the ith detection. Thus, the detections are unlikely due to random noise.

From the deprojected locations, we can estimate the level of t using the observed p. We find that the values are $4.1{\pm}0.9\%$, $9{\pm}3\%$, $15{\pm}5\%$, and $10{\pm}3\%$ where the uncertainty is from error propagation with only the uncertainty from p. When calculating p, we did not remove the free-free component as was done in Carrasco-González et al. (2019) because the free-free emission is only within the central ~ 40 mas and the polarization detections are at least ~ 1 beam ($0.15''$) away from the center. Thus, the detected vectors are unlikely contaminated by free-free emission. Note that a polarization fraction of order 10% is rather high but not unheard of. For example, it is comparable to the 8.1-mm dust continuum polarization of the NGC1333 IRAS4A1 disk (see Fig. 2 of Cox et al. 2015, left panel).

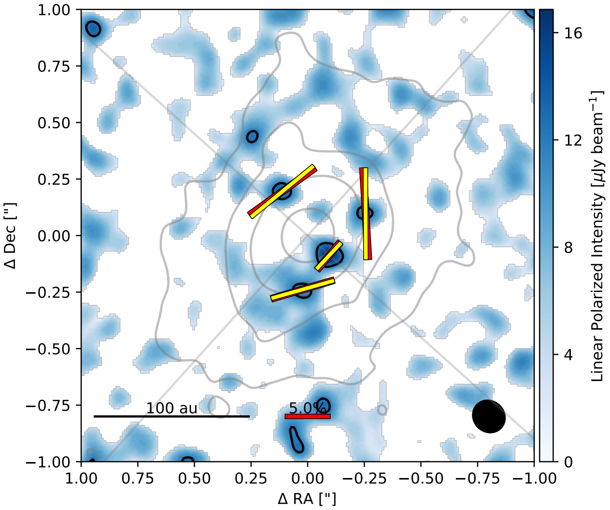

Figure 5. Comparison between the observed polarization direction (red vectors) and the expected polarization direction from toroidally aligned prolate grains (yellow vectors). The lengths are made to match the observed p and only the polarization direction should be compared. The color map is P and the grey contours are the Stokes I in steps of 3, 10, 30, 100, 300, and 1000 σ_I.

5 DISCUSSION

Our main result is that the new ALMA images at Bands 4, 5, and 7 and the VLA Q-band image are consistent with scattering of grains that are effectively prolate and toroidally aligned. This is in line with previous work using just Bands 3, 6, and 7 (Yang et al. 2019; Mori

& Kataoka 2021; Lin et al. 2022). The evidence comes from the increasing azimuthal variation and the decreasing constant component from the ALMA Bands as the wavelength increases from 0.87 mm to 3.1 mm (Sec. 4.2). Though the few marginally detected polarization vectors at the Q-band prohibit analysis of the azimuthal variation, the polarization angles are consistent with the toroidally aligned prolate grains in the optically thin limit as predicted in Lin et al. (2022). From these results, we discuss the implications of the grain structure.

Past studies of HL Tau using (sub)millimeter multiwavelength Stokes I images require large, mm-sized grains by constraining the opacity index $\beta \sim 1$ (Kwon et al. 2011, 2015). Even after accounting for scattering and optical depth effects, Carrasco-González et al. (2019) used resolved ALMA and VLA observations and inferred $\sim$ 1 mm grains. The grain size is in tension with that inferred from polarization studies, which limits the grain size to $\sim$100 μm (e.g. Yang et al. 2016a; Kataoka et al. 2016a).

In Section 4.2, we measured the s-spectrum for the ALMA Bands, which traces the effective contribution from scattering as a function of wavelength. At face value, s falls approximately as $\propto \lambda^{-0.2}$. The weak dependence on λ across 0.87 mm to 3.1 mm is difficult to explain in the simplest case of Rayleigh scattering by small grains, where the scattering polarization efficiency drops much more steeply with increasing wavelength in the optically thin limit. However, this discrepancy can potentially be alleviated by several effects, including the optical depth effects (Lin et al. 2020b, 2022), differential vertical dust settling of grains of different sizes (Ueda et al. 2021, Harrison et al. under review), and differential radial concentration of grains of different sizes in disk substructures (e.g., rings and gaps) that remain unresolved in the polarization data modeled in this paper.

Irregularity of grain structure has been shown to alleviate the tension between the grain sizes inferred from scattering-induced polarization and those from the spectral index (e.g. Shen et al. 2008, 2009; Tazaki et al. 2019; Muñoz et al. 2021; Lin et al. 2023). Indeed, Zhang et al. (2023) simultaneously modeled the Stokes I and the weak λ dependence of polarization of HL Tau assuming porous grains and found that the grains can be greater than 1 mm depending on the porosity.

Aside from the scattering behavior, the lack of any flip in the underlying thermal polarization direction from aligned grains from 870 μm to 7 mm also constrains the grain structure. Compact elongated grains produce thermal polarization following the direction along the projected long axis when λ is much larger than grain size a, or more specifically when $\lambda > 2\pi a$ (Rayleigh regime). However, when λ is comparable to $2\pi a$ (Mie regime), the (thermal) polarization direction can flip, i.e., change by 90°, and become perpendicular to the projected long axis (Kirchschlager et al. 2019; Guillet et al. 2020). At face value, the lack of any flip, even at our shortest wavelength band, implies that the grain size should be smaller than $\sim$ 140 μm. However, as mentioned earlier, it is difficult for such a small grain size to explain the weak λ dependence of the s-spectrum in the simplest case of compact spherical grains in the optically thin limit or the level of Stokes I and P at the VLA wavelengths (see also Ohashi et al. 2020), although the VLA emission is more concentrated towards the inner disk where the dust population could be different from the outer disk where most of the polarization vectors are detected at longer wavelengths.

We should note that, although large (mm-sized) porous grains have the potential to explain the relatively shallow $\lambda-$dependence of the inferred scattering polarization efficiency and the 7 mm emission and polarization observed in the inner disk, they may violate the dipole approximation, Eq. 11, that was used to derive the azimuthal variation of the thermal component of polarization. The extent to which the linear decomposition analysis applies to such grains is unclear. Future efforts to incorporate such grains into detailed modeling for comparison with the multi-wavelength Stokes I and polarization data will be valuable.

6 CONCLUSIONS

We present and analyze multiwavelength polarization observations of the HL Tau disk at Bands 3, 4, 5, 6, and 7 from ALMA and Q-Band from VLA consolidating HL Tau's position as the protoplanetary disk with the most complete wavelength coverage in resolved dust polarization. Our main results are summarized as follows:

(i) New polarization observations using ALMA detected well-resolved polarization at Bands 4, 5, and 7 with angular resolutions of $\sim 0.20''$, $0.17''$, and $0.16''$, respectively. The new VLA Q Band image has a resolution of $\sim 0.15''$ and marginally detects a few polarization vectors. The new data strengthens the case for a smooth systematic transition from unidirectional polarization direction to an azimuthal direction as the wavelength increases.

(ii) The polarization transition is further evidence of scattering prolate grains aligned toroidally in the disk. We disentangle the polarization from scattering and the elongated grains' thermal emission through the azimuthal variation of polarization from a simple model. The constant component from scattering decreases slowly with increasing wavelength, while the thermal component, which causes azimuthal variation, increases with increasing wavelength. The weak dependence of the scattering spectrum is inconsistent with the simplest case of Rayleigh scattering by small grains in the optically thin limit but can be affected by factors such as optical depth, differential vertical and radial concentration of grains of different sizes, and dust porosity.

(iii) The few polarization detections at the Q-band are also consistent with toroidally aligned grains by comparing the expected polarization angles. The polarization fraction is higher, at $\sim 7\%$, and suggests that the intrinsic polarization of grains can be $\sim 10\%$ after correcting for projection of the grain.

ACKNOWLEDGEMENTS

Z.-Y.D.L. acknowledges support from the Virginia Space Grant Consortium (VSGC), NASA 80NSSC18K1095, the Jefferson Scholars Foundation, the NRAO ALMA Student Observing Support (SOS) SOSPA8-003, the Achievements Rewards for College Scientists (ARCS) Foundation Washington Chapter, and UVA research computing (RIVANNA). Z.-Y.L. is supported in part by NASA 80NSSC20K0533 and NSF AST-2307199 and AST-1910106.

This paper makes use of the following ALMA data with project codes: 2016.1.00115.S, 2019.1.00134.S, 2019.1.00162.S, and 2019.1.01051.S. ALMA is a partnership of ESO (representing its member states), NSF (USA), and NINS (Japan), together with NRC (Canada), MOST and ASIAA (Taiwan), and KASI (Republic of Korea), in cooperation with the Republic of Chile. The Joint ALMA Observatory is operated by ESO, AUI/NRAO and NAOJ. The National Radio Astronomy Observatory is a facility of the National Science Foundation operated under cooperative agreement by Associated Universities, Inc.

REFERENCES

ALMA Partnership et al., 2015, ApJ, 808, L3
Alves F. O., et al., 2018, A&A, 616, A56
Andersson B. G., Lazarian A., Vaillancourt J. E., 2015, ARA&A, 53, 501
Aso Y., Kwon W., Hirano N., Ching T.-C., Lai S.-P., Li Z.-Y., Rao R., 2021, ApJ, 920, 71
Bacciotti F., et al., 2018, ApJ, 865, L12
Beckwith S. V. W., Henning T., Nakagawa Y., 2000, in Mannings V., Boss A. P., Russell S. S., eds, Protostars and Planets IV. p. 533 (`arXiv:astro-ph/9902241`), doi:10.48550/arXiv.astro-ph/9902241
Bohren C. F., Huffman D. R., 1983, Absorption and scattering of light by small particles
Carrasco-González C., et al., 2019, ApJ, 883, 71
Contopoulos G., Jappel A., 1974, Transactions of the International Astronomical Union, Volume_XVB: Proceedings of the Fifteenth General Assembly, Sydney 1973 and Extraordinary Assembly, Poland 1973.
Cox E. G., et al., 2015, ApJ, 814, L28
Dent W. R. F., Pinte C., Cortes P. C., Ménard F., Hales A., Fomalont E., de Gregorio-Monsalvo I., 2019, MNRAS, 482, L29
Dolginov A. Z., Mitrofanov I. G., 1976, Ap&SS, 43, 291
Draine B. T., Weingartner J. C., 1997, ApJ, 480, 633
Foreman-Mackey D., Hogg D. W., Lang D., Goodman J., 2013, PASP, 125, 306
Galli P. A. B., et al., 2018, ApJ, 859, 33
Girart J. M., et al., 2018, ApJ, 856, L27
Gold T., 1952, MNRAS, 112, 215
Guillet V., Girart J. M., Maury A. J., Alves F. O., 2020, A&A, 634, L15
Hamaker J. P., Bregman J. D., 1996, A&AS, 117, 161
Hamaker J. P., Bregman J. D., Sault R. J., 1996, A&AS, 117, 137
Harrison R. E., et al., 2019, ApJ, 877, L2
Harrison R. E., et al., 2021, ApJ, 908, 141
Hildebrand R. H., Davidson J. A., Dotson J. L., Dowell C. D., Novak G., Vaillancourt J. E., 2000, PASP, 112, 1215
Hoang T., Lazarian A., 2016, ApJ, 831, 159
Hoang T., Cho J., Lazarian A., 2018, ApJ, 852, 129
Hoang T., Tram L. N., Minh Phan V. H., Giang N. C., Phuong N. T., Dieu N. D., 2022, AJ, 164, 248
Hull C. L. H., Plambeck R. L., 2015, Journal of Astronomical Instrumentation, 4, 1550005
Hull C. L. H., et al., 2018, ApJ, 860, 82
Johansen A., Blum J., Tanaka H., Ormel C., Bizzarro M., Rickman H., 2014, in Beuther H., Klessen R. S., Dullemond C. P., Henning T., eds, Protostars and Planets VI. pp 547–570 (`arXiv:1402.1344`), doi:10.2458/azu_uapress_9780816531240-ch024
Kataoka A., et al., 2015, ApJ, 809, 78
Kataoka A., Muto T., Momose M., Tsukagoshi T., Dullemond C. P., 2016a, ApJ, 820, 54
Kataoka A., et al., 2016b, ApJ, 831, L12
Kataoka A., Tsukagoshi T., Pohl A., Muto T., Nagai H., Stephens I. W., Tomisaka K., Momose M., 2017, ApJ, 844, L5
Kenyon S. J., Gomez M., Marzke R. O., Hartmann L., 1994, AJ, 108, 251
Kenyon S. J., Gómez M., Whitney B. A., 2008, in Reipurth B., ed., , Vol. 4, Handbook of Star Forming Regions, Volume I. p. 405, doi:10.48550/arXiv.0810.1298
Kirchschlager F., Bertrang G. H. M., Flock M., 2019, MNRAS, 488, 1211
Ko C.-L., Liu H. B., Lai S.-P., Ching T.-C., Rao R., Girart J. M., 2020, ApJ, 889, 172
Kwon W., Looney L. W., Mundy L. G., 2011, ApJ, 741, 3
Kwon W., Looney L. W., Mundy L. G., Welch W. J., 2015, ApJ, 808, 102
Lazarian A., Hoang T., 2007, ApJ, 669, L77
Le Gouellec V. J. M., et al., 2020, A&A, 644, A11
Lee H. M., Draine B. T., 1985, ApJ, 290, 211
Lee C.-F., Li Z.-Y., Ching T.-C., Lai S.-P., Yang H., 2018, ApJ, 854, 56
Lee C.-F., Li Z.-Y., Yang H., Daniel Lin Z.-Y., Ching T.-C., Lai S.-P., 2021, ApJ, 910, 75
Lin Z.-Y. D., Li Z.-Y., Yang H., Looney L., Lee C.-F., Stephens I., Lai S.-P., 2020a, MNRAS, 493, 4868
Lin Z.-Y. D., Li Z.-Y., Yang H., Looney L., Stephens I., Hull C. L. H., 2020b, MNRAS, 496, 169
Lin Z.-Y. D., Li Z.-Y., Yang H., Stephens I., Looney L., Harrison R., Fernández-López M., 2022, MNRAS, 512, 3922
Lin Z.-Y. D., et al., 2023, MNRAS, 520, 1210
Lin Z.-Y. D., et al., 2024, MNRAS, 528, 843
Liu H. B., 2019, ApJ, 877, L22
Liu H. B., 2021, ApJ, 914, 25
Loinard L., 2013, in de Grijs R., ed., Vol. 289, Advancing the Physics of Cosmic Distances. pp 36–43 (`arXiv:1211.1742`), doi:10.1017/S1743921312021072
Luhman K. L., 2018, AJ, 156, 271
McMullin J. P., Waters B., Schiebel D., Young W., Golap K., 2007, in Shaw R. A., Hill F., Bell D. J., eds, Astronomical Society of the Pacific Conference Series Vol. 376, Astronomical Data Analysis Software and Systems XVI. p. 127
Morbidelli A., Raymond S. N., 2016, Journal of Geophysical Research (Planets), 121, 1962
Mori T., Kataoka A., 2021, ApJ, 908, 153
Mori T., Kataoka A., Ohashi S., Momose M., Muto T., Nagai H., Tsukagoshi T., 2019, ApJ, 883, 16
Muñoz O., et al., 2021, ApJS, 256, 17
Ohashi S., et al., 2020, ApJ, 900, 81
Perley R. A., Butler B. J., 2013, ApJS, 206, 16
Pinte C., Dent W. R. F., Ménard F., Hales A., Hill T., Cortes P., de Gregorio-Monsalvo I., 2016, ApJ, 816, 25
Roccatagliata V., Franciosini E., Sacco G. G., Randich S., Sicilia-Aguilar A., 2020, A&A, 638, A85
Sadavoy S. I., et al., 2019, ApJS, 245, 2
Shen Y., Draine B. T., Johnson E. T., 2008, ApJ, 689, 260
Shen Y., Draine B. T., Johnson E. T., 2009, ApJ, 696, 2126
Steinacker J., Baes M., Gordon K. D., 2013, ARA&A, 51, 63
Stephens I. W., et al., 2014, Nature, 514, 597
Stephens I. W., et al., 2017, ApJ, 851, 55
Stephens I. W., Fernández-López M., Li Z.-Y., Looney L. W., Teague R., 2020, ApJ, 901, 71
Stephens I. W., et al., 2023, Nature, 623, 705
Takahashi S., Machida M. N., Tomisaka K., Ho P. T. P., Fomalont E. B., Nakanishi K., Girart J. M., 2019, ApJ, 872, 70
Tang Y.-W., et al., 2023, ApJ, 947, L5
Tazaki R., Tanaka H., Kataoka A., Okuzumi S., Muto T., 2019, ApJ, 885, 52
Ueda T., Kataoka A., Zhang S., Zhu Z., Carrasco-González C., Sierra A., 2021, ApJ, 913, 117
Vaillancourt J. E., 2006, PASP, 118, 1340
Valdivia V., Maury A., Hennebelle P., 2022, A&A, 668, A83
Yang H., Li Z.-Y., Looney L., Stephens I., 2016a, MNRAS, 456, 2794
Yang H., Li Z.-Y., Looney L. W., Cox E. G., Tobin J., Stephens I. W., Segura-Cox D. M., Harris R. J., 2016b, MNRAS, 460, 4109
Yang H., Li Z.-Y., Looney L. W., Girart J. M., Stephens I. W., 2017, MNRAS, 472, 373
Yang H., Li Z.-Y., Stephens I. W., Kataoka A., Looney L., 2019, MNRAS, 483, 2371
Yen H.-W., et al., 2017, A&A, 608, A134
Zhang S., Zhu Z., Ueda T., Kataoka A., Sierra A., Carrasco-González C., Macías E., 2023, ApJ, 953, 96
Zhu Z., et al., 2019, ApJ, 877, L18

This paper has been typeset from a TEX/LATEX file prepared by the author.